Nano Energy 78 (2020) 105246

Contents lists available at ScienceDirect

Nano Energy

journal homepage: http://www.elsevier.com/locate/nanoen

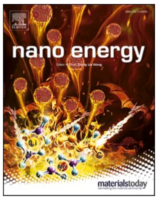

# A self-powered artificial retina perception system for image preprocessing based on photovoltaic devices and memristive arrays

Xiaoyang Yang [a], Ziyu Xiong [b], Yongji Chen [c], Yi Ren [d], Li Zhou [a], Huilin Li [a], Ye Zhou [d,**], Feng Pan [c], Su-Ting Han [a,*]

[a] Institute of Microscale Optoelectronics, Shenzhen University, 3688 Nanhai Road, Shenzhen, 518060, PR China
[b] College of Physics and Optoelectronic Engineering, Shenzhen University, 3688 Nanhai Road, Shenzhen, 518060, PR China
[c] School of Advanced Materials, Peking University Shenzhen Graduate School, 2199 Lishui Road, Shenzhen, 518055, PR China
[d] Institute for Advanced Study, Shenzhen University, 3688 Nanhai Road, Shenzhen, 518060, PR China

ARTICLE INFO

*Keywords:*
Self-powered
Artificial retina
Perovskite
Memristor
Neuromorphic computing

ABSTRACT

Artificial retina perception system is significant to pattern recognition and visual function emulation. However, the recent artificial retina system is mainly reported on the integration of three-terminal transistors, whose structural limitations may result in low processing speeds and high energy consumption due to a low array density and complex line design. Furthermore, the external power source is required to drive devices so that the power consumption of the system would increase. Here we present a self-powered artificial retina perception system by utilizing two-terminal solar cells as artificial neurons and perovskite-based memristors as artificial synapses, ensuring the bio-inspired retina system with extendable crossbar array structure for high-density and low power consumption neural networks. By a light stimulation with various wavelengths and intensities, the electrical pre-synaptic signal is generated in the solar cell and subsequently transferred to the perovskite-based memristor to perform further information preprocessing. Especially, the applicability of the artificial retina system to neuromorphic computing is demonstrated for contrast enhancement and noise reduction. The retina perception system is capable of feature extraction by to implement partial functions of convolutional neural networks (CNNs) on the hardware level with improved recognition rate, boosted recognition speed, and reduced energy consumption.

## 1. Introduction

Motivated by the mammalian eyes, the artificial visual perception system has attracted enormous interests due to its potential application to emulate neuromorphic functionalities such as pattern recognition, learning, and memorization for future artificial intelligence [1–6]. In the first part of biologically visual system, the retina with layers of neurons connected by synapses could transform incident visible photons into neural signals and communicated to the brain for image construction. The preprocessing function of biological retina for further parallel and hierarchical processing is of great significance due to its efficacy to eliminate the useless input information, economize the memory space and reduce the computational work of neural networks which give direct inspiration of convolutional neural networks (CNNs) [7,8]. Hardware emulating the biological retina perception system acquires the integration of photodetectors functioning as neurons and artificial synapse with various synaptic behavior [9–12]. The photodetectors ensure the capturing of visual information by translating the light signals into pre-synaptic electrical signal [13–19]. By integrating artificial synapses with short-term plasticity (STP) and long-term plasticity (LTP), first-stage data processing and memory can be achieved [4].

Recently, the integration of the three-terminal transistor based photosensor and synapse to resemble artificial retina system has attracted considerable attention due to their nondestructive read-out behavior, which is attributed to the completely separated terminals for reading (drain) and writing (gate) [5]. The sensing transistor such as optoelectronic organic thin film transistor connected with neuromorphic transistor, including electrochemical transistor and flash memory, has been reported to fabricate bio-inspired visual perception systems [5]. However, the structural limitations of these three-terminal

---

* Corresponding author.
** Corresponding author.
*E-mail addresses:* yezhou@szu.edu.cn (Y. Zhou), sutinghan@szu.edu.cn (S.-T. Han).

https://doi.org/10.1016/j.nanoen.2020.105246
Received 21 May 2020; Received in revised form 23 July 2020; Accepted 30 July 2020

devices, such as a low array density and complex line design, may result in low processing speeds and high energy consumption of the entire system [20]. Furthermore, the external power source is required to drive the optical sensor and artificial synapse so that the power consumption of the system would increase [11,21].

Utilizing the two-terminal structure of self-powered photodetectors as artificial neurons and memristors as artificial synapses ensures the bio-inspired retina system to be extendable to crossbar array structure for high-density and low power consumption neural network, while which has not been realized yet. In this work, we designed a self-powered artificial retina system via the integration of silicon solar cells and halide perovskite memristors. The two-terminal structure of both photovoltaic cells and memristors ensures the bio-inspired retina system to be extendable to crossbar array structure for high-density neural networks. The artificial retina perception system could be self-powered and exhibit broadband response ranging from visible and near-infrared light due to the excellent photovoltaic conversion capability of polycrystalline silicon solar cells. With the modified structure of ITO/$CsPbBr_2I$/poly(3-hexylthiophene) (P3HT)/Ag, both the low operating voltage of $\sim$ 0.4 V and the decay process of perovskite-based memristor was realized, allowing the bi-modal STP-LTP functionality and efficiently light-initiated weight-updating process. By a light stimulation with various wavelengths and intensities, the electrical output signal is generated in the solar cell and subsequently transferred to the perovskite-based memristor to perform information preprocessing. Especially, through real-time training and testing processes, the applicability of the artificial retina system to neuromorphic computing is demonstrated for the contrast enhancement and noise reduction. The retina perception system is capable of feature extraction and classification by elementary devices to complete partial functions of CNNs with improved recognition rate, boosted recognition speed, and reduced energy consumption. High recognition rate of $\sim$ 86% can be implemented within 180 training epochs after the introduction of our self-powered artificial retina perception system. The proposed self-powered artificial retina system is expected to be an important steppingstone to the development of the internet of things and edge computing.

## 2. Experimental section

### 2.1. ITO/perovskite/P3HT/Ag memristor fabrication

ITO transparent conducting substrates were cleaned by sequential 30 min sonication in warm deionized water, acetone, and isopropanol. After being dried under a nitrogen flow at atmospheric pressure, the substrates were treated with UV-ozone for 10 min. The perovskite $CsPbBr_2I$ precursor solution was immediately spin-coated onto the substrate at 500 rpm for 5 s, then 2000 rpm for 30 s. The perovskite $CsPbBr_2I$ precursor solution was formed by mixing 0.461 g of $PbI_2$, 0.367 g $PbBr_2$ and 0.425 g of CsBr into 4 mL dimethyl sulfoxide (DMSO) and N,N-dimethylformamide (DMF) mixed solvent ($V_{DMSO}$:$V_{DMF} = 1$:1). The P3HT solution was then spin-coated on the perovskite layer and the combination was baked at 100 °C for 20 min. Finally, 100 nm of Ag was deposited as top electrode by thermal evaporation.

### 2.2. Polycrystalline silicon solar cells fabrication

Semi-finished devices with a $SiN_x$/n-Si/p-Si/Al configuration were bought from Tian-Si New Energy Company. DuPont PV18H silver paste was screen-printed on semi-finished devices. Then calcination process was performed in a seven-section meshbelt furnace, which was designed by ourselves and assembled by Hefei Ke-Jing Materials Technology Company.

### 2.3. Film and device characterization

The crystal structure of $CsPbBr_2I$ films were certified using a Bruker D8 Advance powder X-ray diffractometer equipped with Cu K$\alpha$ radiation with a two-dimensional detector. The scan range of 2$\theta$ was from 5 to 50°, and the scan step of 2$\theta$ was 0.02°.

The morphology of thin films and the interface of ITO/Perovskite/P3HT/Ag memristor were captured using a field emission scanning electron microscope (Carl Zeiss MERLIN Compact).

The infrared transmittance spectra were carried out by FT-IR spectrometer (PerkinElmer, Frontier).

The interface of Perovskite/P3HT/Ag was analyzed by transmission electron microscope (TEM, FEI Tecnai G2 F30). The energy dispersive X-ray spectroscopy (EDX) was employed to analyze the element distribution of C, Br and I. The sample of the interface of Perovskite/P3HT/Ag for TEM was prepared by Focused Ion Beam (FIB, FEI, Scios) followed by Ion Beam Modulating.

The *I–V* curves and the synaptic functions for the memristor were conducted by a semiconductor parameter analyzer (Keysight B2902A). Electrical bias was applied to the TE while the BE was grounded. The synaptic plasticity such as SVDP, SDDP, SFDP, PPF index, ITDP, IIDP, and IWDP were tested with each condition using three devices whose initial states were proved to be close by a reading voltage of 0.01 V. Then, the averaged value was calculated and used from the data of three devices.

The EQE of Polycrystalline silicon solar cells was tested by a QE measurement system (ABET TECHNOLOGIES, AB6000).

Synaptic functions under different irradiation intensity and wavelength were achieved by a solar simulator (Zolix, 150W), and a tunable-power LEDs source (LASERWAVE, CLASS IV), respectively. The irradiation intensity was certified by a laser power meter (Beijing Yanbang, VLP-2000), which was calibrated by a standard silicon reference solar cell.

## 3. Results and discussion

### 3.1. Design of self-powered artificial retina system, device fabrication and characterization

The biological visual system contains the retina, optic nerves and the visual center (Fig. 1A: a). Neurons in the retina such as rods and corns, playing a role as visual perception receptor, could receive and convert external optical signals into electrical signals through photonic-to-electronic conversion. Then these signals were transferred to bipolar retinal cells by electronic-to-ionic conversion (synapses in Fig. 1A: b) [22]. Subsequently, synapses readout, process and memorize the signal from neuron with synaptic plasticity (Fig. 1A: c). After information preprocessed by the retina, visual signals are then sent to the primary visual cortex, or the V1 area, relayed by the lateral geniculate nucleus (LGNs) (Fig. 1A: a). The visual center is information processing and recognition center, and finally implements learning and forms memorization.

Our self-powered artificial retina perception system is composed of photodetectors and artificial synapses. It could sense information which is analogue to light-tunable neural signals with time-dependent plasticity, allowing the partial CNN functions of image processing, such as noise reduction (Fig. 1A: d). The photodetector in our system is based on two-terminal silicon solar cells to serve as rods and cones in the artificial retina for receiving the external optical signals and converting them into electrical signals (Fig. 1A: e) [23]. Artificial synapses in our system are based on perovskite-based memristors. Perovskite-based memristors connecting with solar cells are then powered by photovoltaic energy harvested from the input light to work as optic-neural synapses (Fig. 1A: f). In our perovskite-based synaptic devices, the TE and BE respectively serve as pre-synaptic input and post-synaptic output, while the change of conductance/resistance of halide perovskite film is regarded as the potentiation or depression of the synaptic weight. Therefore, after light signals being transformed into pre-synaptic spikes to stimulate the memristor, the post-synaptic current companied with changes of the

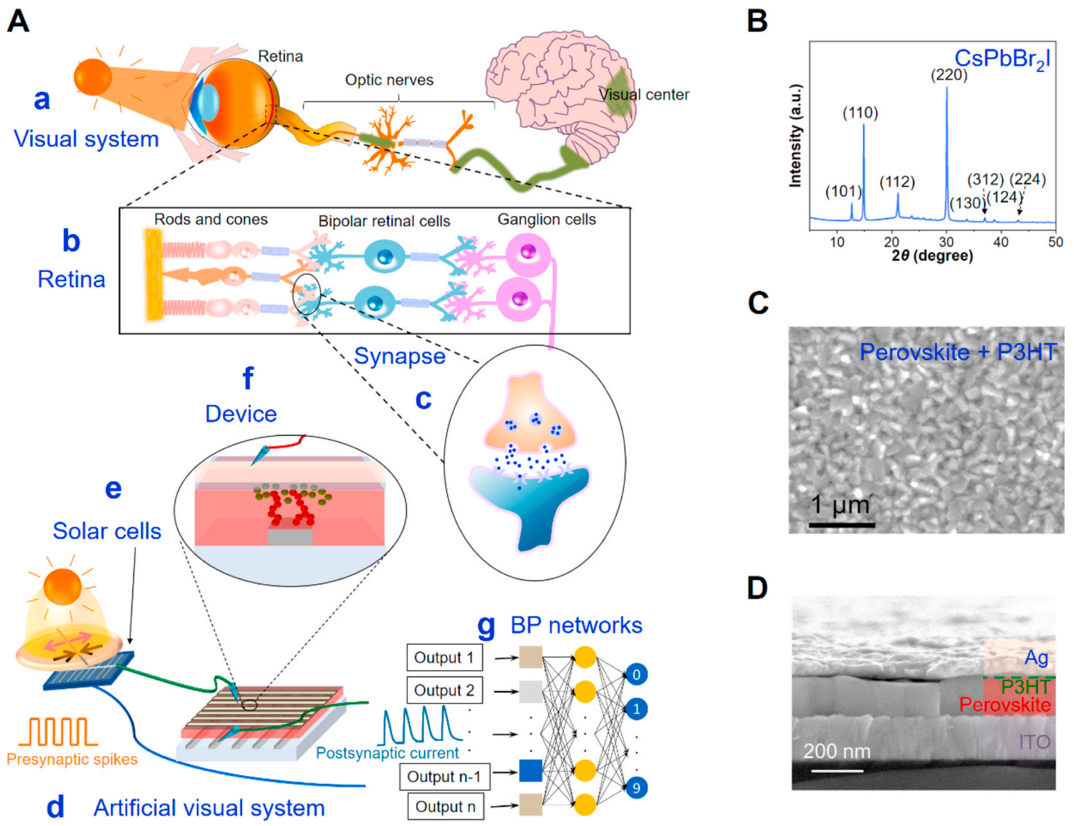

**Fig. 1.** Design of Self-powered Artificial Retina System, Device Fabrication and Characterization. (A) The biological and artificial visual system. a: The biological visual system consisting of the retina (receiving and preprocessing), optic nerves (transmitting), and the visual center (processing and memory system); b: a schematic image of the retina; c: the schematic illustration of biological synapses between rods (or cones) and bipolar retinal cells; d: the artificial visual system consisting of solar cells (working as the retina), perovskite memristors (working as synapses), and ANNs (working as the visual center); the output of post-synaptic current can secondarily input into ANNs; e: solar cells; f: devices with conductive filaments; g: ANNs. (B) XRD spectra of perovskite films spin-coated on glass substrate with peaks assigned to the orthorhombic phase. (C) Top-view SEM images of annealed perovskite films with P3HT passivation. (D) A cross-sectional SEM image of ITO/CsPbBr$_2$I/P3HT/Ag memristors.

conductance/resistance of perovskite-based memristors can be obtained. Finally, the post-synaptic current can be secondarily input into artificial neural networks (ANNs) which work as the visual center (Fig. 1A: g). The pattern recognition is achieved in ANNs by the gradient descent iteration method.

Memristive devices based on halide perovskites have drawn great attention owing to the feasibility of low-cost solution processing and excellent memristive behavior arising from their intrinsic ionic migration characteristics (briefly summarized in Table S1) [24–31]. In terms of plasticity timescale, synapses with LTP and STP signify the neural foundation for memory formation and experience acquisition. However, the second-to-minute level of LTP time scale of non-passivated memristor limits their implementation as reliable STP-LTP devices [32]. First, to obtain reliable synaptic functions, the structure of perovskite synaptic memristor was delicately designed as ITO/CsPbBr$_2$I/P3HT/Ag (shown in Fig. S1). The perovskite CsPbBr$_2$I was used as active layer because of the unstability of CsPbI$_3$ and the low ON/OFF ratio of CsPbBr$_3$ devices [33,34]. The perovskite CsPbBr$_2$I precursor solution was spin-coated to form an active layer. Then an ultrathin P3HT layer was deposited onto the perovskite layer to passivate the surface of perovskite film. Finally, 60 nm Ag TE was evaporated to obtain crossbar arrays. The Ag electrode was employed instead of the Au electrode in memristors due to the low operating voltage of ITO/Perovskite/Ag devices (Table S1).

The perovskite film was confirmed to be the orthorhombic phase via a standard X-ray diffraction (XRD) patterns analysis (Fig. 1B). The peaks at $2\theta = 12.66$, 14.86, 21.16, 30.07, 33.78, 37.03, 38.78 and 43.16 are assigned to the (101), (110), (112), (220), (130), (312), (124) and (224) planes of the orthorhombic phase (ICDD: 01–02707929) of the perovskite, respectively. Similar results can be found in the previous reports [35]. According to the top-viewed scanning electron microscope (SEM) images (Fig. S2), perovskite films exhibit high-surface coverage with small grain size less than 300 nm which exhibits negligible variation after P3HT passivation (Fig. 1C). The thickness of the perovskite layer is verified by the cross-sectional SEM to be ~ 150 nm (Fig. 1D) while the P3HT layer is too thin to be directly distinguished by SEM. The existence of P3HT passivation layer was verified by the infrared transmittance spectra (Fig. S3). Compared with the non-passivated perovskite film, the P3HT passivated perovskite film shows evolutionary absorption peaks in Region A (1460 cm$^{-1}$) and Region B (2853 and 2924 cm$^{-1}$) which are assigned to the C–H asymmetric bending vibration (1460 cm$^{-1}$) and stretching vibration (2853 and 2924 cm$^{-1}$) in (-CH$_2$-) of P3HT [36].

### 3.2. *Effect of passivation process on synaptic plasticity of memristors*

The typical current-voltage (*IV*) curves of the perovskite-based devices with and without P3HT passivation by grounding the ITO (BE) and exerting the voltage on the top Ag electrode (TE) are obtained as displayed in Fig. 2A and 2B. Different from devices which show sudden conductance variation in resistive random access memories (RRAMs) with binary states, the conductance of perovskite-based memristor varies gradually under both positive and negative sweeps which are fingerprint for synaptic memristors. Devices without P3HT-passivation present memristive characteristics with almost no hysteresis (ON/OFF ratio ~ 1.2) and limited conductivity states (Fig. 2A). After passivating with P3HT, the hysteresis opens (ON/OFF ratio > 10) in the *IV* curve of

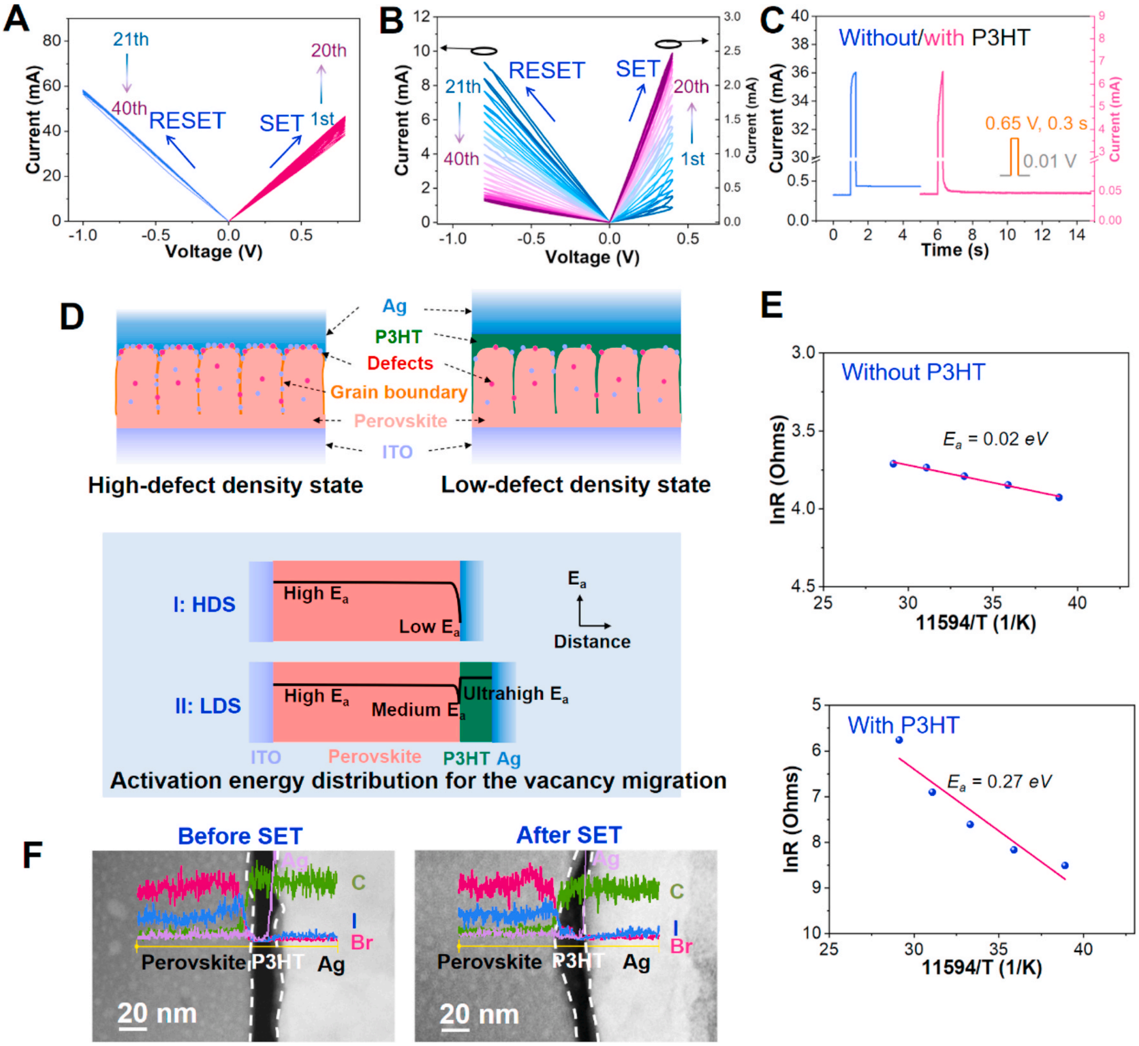

**Fig. 2.** Effect of Passivation Process on Synaptic Plasticity of Memristors. The memristive characteristics of the perovskite-based memristors without (A) and with (B) the P3HT-passivated process induced by setting and resetting processes. (C) EPSC triggered by an applied external pulse for the perovskite-based memristors without (blue) and with (pink) the P3HT-passivated layer. (D) Top: The schematic diagram of high-defect density state (HDS) and low-defect density state (LDS) for perovskite-based memristors before (left) and after (right) P3HT passivation. The red and blue points represent antisite defects and under-coordinated $Cs^+$ ions, respectively. Below: The schematic diagram of activation energy distribution for the ion migration in perovskite-based memristors under HDS or LDS condition. (E) Arrhenius plots of resistance in perovskite-based memristors without (top) and with P3HT-passivated layer. Activation energy of halogenic ions was calculated by fitting the linear region. (F) TEM images and EDS profiles of the cross-section of perovskite devices before (left) and after (right) applying a SET process to form LTP (yellow line: position EDS line profile).

devices and the conductivity states can be tuned in a much wider range (Fig. 2B). Those phenomena may attribute to the eliminated Ag penetration from perovskite films during vacuum evaporation and reduced initial operating current for P3HT-passivated devices. Contrastively, P3HT-only devices almost have no memristive behaviors (Fig. S4). Significantly, P3HT-passivated perovskite-based devices could achieve a low and narrow-distributed SET voltage around 0.4 V. When consecutive negative sweeps from 0 to - 0.8 V were applied, the decreased current trend could be observed during RESET processes. In addition, P3HT-passivated perovskite-based devices show good stability, reliability (good device yield > 98%) and uniformity (Figs. S5 and S6). Most of P3HT passivated devices can perform well after preserving in glovebox for four months (Fig. S5). However, when the P3HT is too thick, memristors will have high operating voltage of >1.2 V and be unsuitable to be powered by solar cells (Fig. S4).

In our synaptic memristors, the TE and BE are analogues of the presynaptic and postsynaptic neuron terminals, respectively. The excitatory postsynaptic current (EPSC) of the memristor triggered by the presynaptic spikes is perceived as the change of synaptic weight, because the real-time change of resistance/conductivity can be presented for memristors. After electrical stimulation applying electrical pulse with the amplitude of 0.65 V and the duration of 0.3 s, for the non-passivated memristor, the excitatory postsynaptic current (EPSC) first increases sharply to a much higher current level than the base line which can be explained that a temporary formation of halogenic vacancy ($V_{Br}^{+1}$ and $V_{I}^{+1}$) conduction channel [37]. Subsequently, the EPSC suddenly drops back to its lower state due to the back-diffusion of halogenic ions. This current decreasing is very fast without decay process and cannot recover to its original states (Fig. 2C). It should be noting that non-passivated perovskite memristor with such electrical performance is hard to be modulated consecutively to realize synaptic plasticity and STP-LTP transition by adjusting the amplitude/frequency of voltage pulses. While after passivating with a thin P3HT layer, perovskite memristors exhibit the obvious decay process of EPSC which could return to its original states after removal of external bias, which ensures the STP-LTP functions for efficient weight-updating (Fig. 2C).

These results led us to hypothesize that P3HT passivation not only influences halogenic ion (Br and I) migration rate, but also inhibits the reaction between the Ag electrode and the halogenic ion (Br and I) for the possible formation of silver halides. First, the occurrence of decay process in P3HT-passivated perovskite device stems from the slow rupture of halogenic vacancy ($V_{Br}^{+1}$ and $V_{I}^{+1}$) conductive filaments due to the sleepy back-diffusion of halogenic ions. According to the Arrhenius equation: $k = \frac{k_B T}{h} e^{-\frac{E_a}{RT}}$, where $k_B$ is the Boltzmann constant, $T$ is the temperature, $h$ is the reduced Planck constant, $E_a$ stands for the activation energy of ions, and $R$ represents the ideal gas constant [38], the decay process of synaptic devices is positively correlated to the $E_a$ of halogenic ions. The activation energy distribution of the halogenic vacancy is presented in Fig. 2D. There are many positively charged defects such as under-coordinated $Cs^+$ ions ($V_{Br}^{+1}$ and $V_{I}^{+1}$) and antisite defects ($Br_{Pb}^{+3}$ and $I_{Pb}^{+3}$) in the perovskite crystal. These positively charged defects mainly distribute on the surface of perovskite crystals and induce high-defect density state (HDS), which could provide many available trapping sites for halogenic ions to form conductive switching filaments. Therefore, the $E_a$ is low on the surface of perovskite crystals (Fig. 2D: I, HDS). After passivated by P3HT, positively charged defects on the surface of perovskite crystals decrease, so that available sites for halogenic ions migration decrease to induce a medium value of $E_a$ (Fig. 2D: II, low-defect density state (LDS)). In P3HT layer, available sites are very limited so that the highest $E_a$ is achieved. The average $E_a$ in perovskite-based devices could be calculated to support our hypothesis (Fig. 2E). When the temperature changed gradually, the $E_a$ could be acquired by fitting Arrhenius plots according to the equation: $lnR(T) = lnR_0 + \frac{E_a}{kT}$ [39,40]. In this equation, $R$ is the resistance, $R_0$ is the pre-exponential factor, $k$ represents the Boltzmann constant, and $T$ is the absolute temperature. The average $E_a$ are calculated to be 0.02 and 0.27 eV for perovskite-based devices without and with P3HT-passivated layer, respectively. The ions with higher $E_a$ migrate much slowly to induce the sluggish formation and rupture processes of conductive filaments and subsequently decay process, so P3HT-passivated perovskite devices have the capacity of realizing synaptic plasticity and STP-LTP transition.

Furthermore, as halogenic ions migrating to contact with the silver electrode in non-passivated perovskite-based memristors under external bias, the possible formation of silver halide makes the EPSC hard to return to its initial state [41]. The P3HT layer could serve as a reservoir to trap mobile ions and suppress the formation of silver halide during the SET process [42]. As demonstrated in Fig. 2F and Fig. S7, energy dispersive spectroscopy (EDS) line profiles of transmission electron microscope (TEM) images (Fig. S8) were employed to detect halogen in perovskite and P3HT layers. Before a set process, there are few halogens in P3HT layer (Fig. 2F: left). Comparatively, halogenic ions can be detected in the P3HT layer after the set process (Fig. 2F: right). There is no clear observation of voltage-induced migration of $Ag^+$ ion. This result also proves that memristive characteristics are contributed from the migration of halogenic ions.

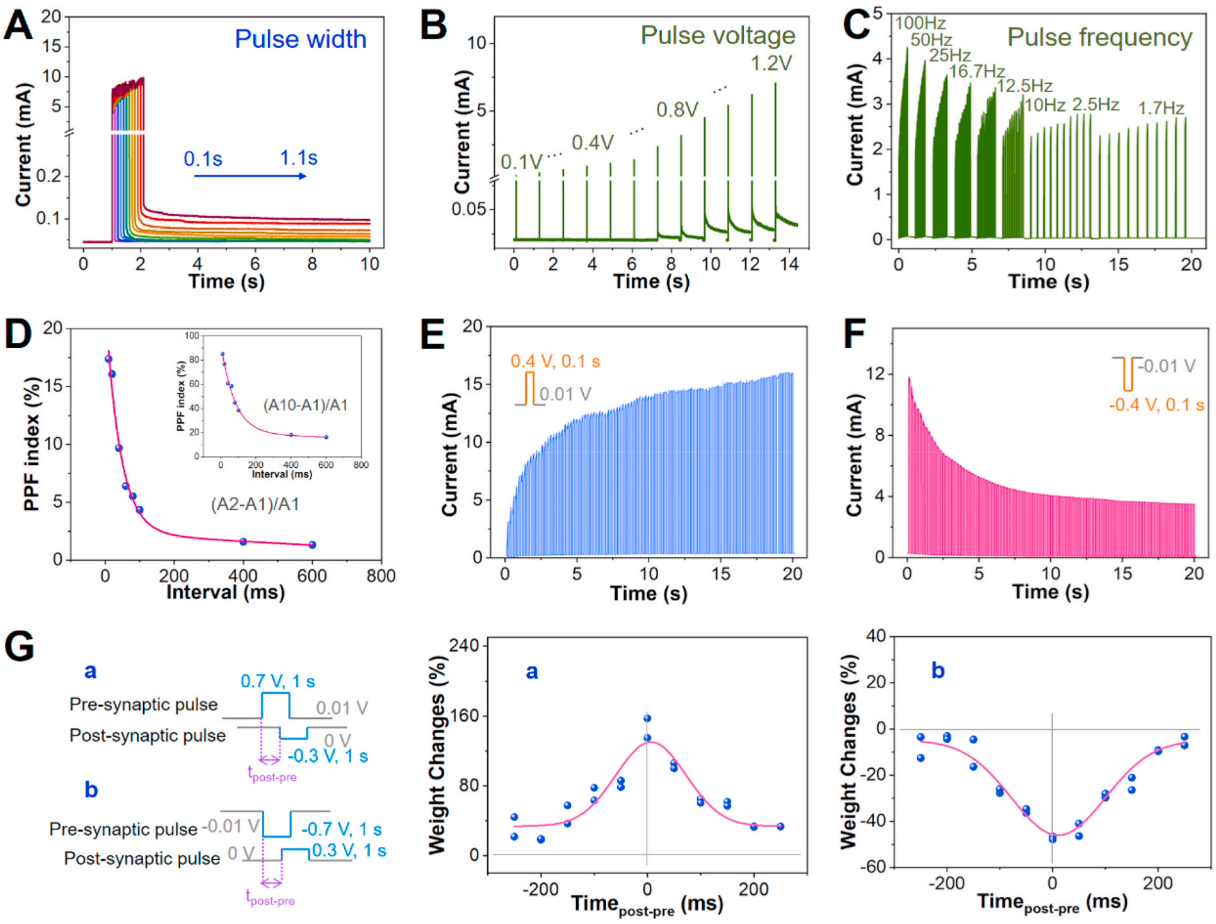

**Fig. 3.** Synaptic Plasticity of Perovskite-based Artificial Synapses. (A) EPSC according to the pulse duration from 0.1 to 1.1 s (spike amplitude: 0.65 V). (B) EPSC according to the pulse voltage amplitude from 0.1 to 1.2 V (spike duration 0.5 ms). (C) EPSC according to the pulse frequency from 1.7 to 100 Hz. (D) PPF index versus time interval between two successive pulses (−0.45 V, 0.05 s duration). Inset: PPF index versus time interval between the 1st and the 10th pulse (−0.45 V, 0.05 s duration). (E) Emulated EPSC plasticity using positive pulses (0.4 V; pulse width, 0.1 s; pulse interval, 0.1 s). (F) Emulated EPSC plasticity using negative pulses (−0.4 V; pulse width, 0.1 s; pulse interval, 0.1 s). (G) Implementation of STDP-like behaviors in the perovskite-based artificial synapses: the symmetric Hebbian rule (a), and the symmetric anti-Hebbian rule (b). The blue dots demonstrate the experimental data and the pink lines are fitting to dots. The left diagram reveals pre-synaptic and post-synaptic spikes.

### *3.3. Synaptic plasticity of perovskite-based artificial synapses*

The P3HT-passivated perovskite memristor can be programmed with history-dependent resistance states and reliable state-maintenance capability, which allows us to emulate the learning and memory functions of the human brain including STP and LTP by controlling the duration/amplitude/frequency of input voltage. Fig. 3A shows the EPSC under electrical stimuli with a fixed amplitude of 0.65 V and different pulse width ranging from 0.1 s to 1.1 s. The peak value of EPSC gradually increases as the pulse width increases, indicating that a longer duration for a single stimulus will result in larger synaptic weight, that is, the higher synaptic connection strength could be achieved. This characteristic of the perovskite-based artificial synapse is also known as spike-duration dependent plasticity (SDDP) [40]. As shown in Fig. 3B, under fixed pulse width, EPSC gradually increases as the amplitude of voltage increases, implying that perovskite-based artificial synapse has the function of spike-voltage dependent plasticity (SVDP). The STP-LTP transition can be achieved by stimulating the device with longer duration than 0.5 ms and higher voltage than 0.8 V. While non-passivated memristors exhibit no decay process of EPSC even though input voltage varies in the wide range (Fig. S9).

The spike-frequency dependent plasticity (SFDP) of perovskite-based synaptic devices is known as an extended form of Hebbian learning, which is closely related to learning, associative memory, and forgetting [43,44]. In biological synapses, the second stimulus will be enhanced by the first stimulus within a short interval, when consecutive stimuli are exerted. Analogously, the second change of film conductivity is also dependent on the paired-pulse interval ($\Delta t$) in perovskite-based artificial synapses. Ten synaptic spikes with various frequencies (1.7 to 100 Hz) were applied to devices and evaluated the paired-pulse facilitation (PPF) for STP of the artificial synapse (Fig. 3C and Fig. S10). When the spike frequency enhances, the EPSC increases because of the accelerated ion migration and the suppressed ion back-diffusion under the high-rate pulses. The relation of synaptic weight change and $\Delta t$ is commonly evaluated by a PPF index as described in Fig. 3D. The PPF index can be calculated from equation (A2-A1)/A1, where A1 and A2 are the peak value of the first and second pulse responses, respectively. The PPF increases from 1.3% to 17.4%, as $\Delta t$ decreased from 600 to 10 ms. Then the data was fitted with the equation of double-exponential function: $PPF = C_1 \exp\left(-\frac{t}{\tau_1}\right) + C_2 \exp\left(-\frac{t}{\tau_2}\right)$ [45]. The characteristic time constants of the rapid ($\tau_1$) and slow ($\tau_2$) phases are fitted to be 0.042 and 1.79 s.

Fig. 3E illuminates a continuous long-term potentiation process of the postsynaptic current with the accumulation of spike number in which the 100 times repeated training process of the positive spike (spike magnitude, 0.4 V; spike width, 100 ms; spike interval, 100 ms) was carried out. The postsynaptic current increases from 0.9 to 16.0 mA. The continuous long-term depression process is also conducted through the 100 times repeated training process of the negative spike (spike magnitude, −0.4 V; spike width, 100 ms; spike interval, 100 ms). The current decreases gradually from 11.8 to 3.5 mA, as presented in Fig. 3F. In the biological neuron system, the potentiation effect is helpful to the learning and memory process. The depression effect also plays a significant role in selectively forgetting weak specific synapse [46].

Spike-time-dependent plasticity (STDP) can evaluate temporal correlations between the pre-synaptic and post-synaptic spikes which is considered as one pivotal rule of Hebbian learning [43,47]. Based on Hebb's theory, the connection strength of synapse becomes stronger, when two neurons simultaneously receive stimuli. Generally, the STDP illustrates the time-dependent relationship between the spikes and the connection strength of the synapse. The connection strength shows characteristic variation when a presynaptic spike precedes/lags the postsynaptic spike. Thus, it can significantly affect the long-term synaptic modification. In biological synapses, various forms of STDP are verified with different functions referring to the information processing and storage [48]. First, the presynaptic spike (spike magnitude, 0.7 V; spike width, 1 s) and the postsynaptic spike (spike magnitude, −0.3 V; spike width, 1 s) generated by the semiconductor analyzer are applied to our artificial synapse to achieve the symmetric Hebbian learning rule (Fig. 3G: a and Fig. S11) [28,49,50]. When two stimuli occur simultaneously ($\Delta t = 0$, $\Delta t = t_{\text{post}} - t_{\text{pre}}$), the synaptic weight ($\Delta W$) obtain the largest enhancement compared with other conditions, indicating the formation of the strongest synaptic connection. When the pre-synaptic spike precedes the postsynaptic spike ($\Delta t > 0$) or lags the postsynaptic spike ($\Delta t < 0$), all synaptic weight variations ($\Delta W$) weaken as the interval increases. The symmetric anti-Hebbian learning rule is also achieved by applying the reverse presynaptic spike (spike magnitude, −0.7 V; spike width, 1 s) and the reverse postsynaptic spike (spike magnitude, 0.3 V; spike width, 1 s). The similar result was observed with the depressed synaptic weight instead of the excited one for the symmetric anti-Hebbian learning case (Fig. 3G: b). The relationship between $\Delta W$ and $\Delta t$ can be fitted by the Gaussian function $\Delta W = \mathrm{A}e^{\frac{-\Delta t^2}{2\tau^2}} + W_0$ [51]. In this equation, A and $\tau$ stand for the scaling factor and time constant of the exponential function, respectively. The $\tau$ is calculated to be 66 and 89 ms in the symmetric Hebbian and anti-Hebbian learning case, respectively.

### *3.4. Synaptic plasticity of artificial synapses powered by solar cells*

Next, P3HT-passivated perovskite synaptic memristors were connected with silicon solar cells to fabricate the self-powered artificial retina system. Recently, the self-powered design to harvest energy from a locally available source, such as piezoelectric and triboelectric devices [52], biofuel cells [53,54], thermoelectric devices [55], and photovoltaic cells [56–59], has a rapid growth in electronics. Generally, a full-sun intensity (100 mW/cm$^2$) was used for solar cells in these self-powered systems, including those providing power for both electronic devices and capacitors [56–59]. Si solar cells are employed to power memory and synaptic devices by converting the external light to the electricity in our system. Solar cells act as diodes and have rectification effects, which may make reduce sneak path in crossbar arrays [60]. Exposure to the light source induces the solar cell to generate a voltage spike. The open-circuit voltage ($V_{\text{oc}}$) of Si solar cells is of $\sim$ 0.5 V under simulated solar irradiation with various light intensities (Fig. S12a), while $V_{\text{oc}}$ is of $\sim$ 0.4 V under illumination with various wavelengths and a fixed intensity of 40 mW/cm$^2$ (Fig. S12b). The variation of $V_{\text{oc}}$ is originated from the parallel resistance effect which is nonnegligible since the photocurrent density is low [61]. When powering the circuit, our solar cells can supply positive voltages from their back-aluminum electrodes or negative voltages from their front-silver electrodes. The perovskite-based memristor acts as the synapse between rods (or cones) and bipolar retinal cells (Fig. 4A). Similar to being driven by electrical power, the top electrode, the perovskite film, and the bottom electrode of perovskite-based memristors play roles of the pre-synapse, the synaptic connection strength, and the post-synapse in synapses, respectively. As schematized in Fig. 4B, a shutter was used to control light input. When the light acts on a photovoltaic cell, the photovoltaic energy generates and its back-aluminum electrode provides positive voltage as pre-synaptic stimuli for the TE of perovskite-based memristors [27,29]. Simultaneously, the output current can be detected, collected and recorded by a device current waveform analyzer. The change of synaptic weight can be detected and calculated from the pre-spike and post-spike current by a low read voltage of 0.01 V. The test system for our self-driven artificial optic-neural system composed of solar cells and memristors is shown in Fig. S13.

The irradiation-time-dependent plasticity (ITDP) of artificial optic-neural synapses which is corresponding to the response of eyes with the quick glance or the long gaze was then resembled by the self-driven artificial retina system (Fig. 4C). The output current increases as the increased irradiation time. In addition, longer irradiation time was

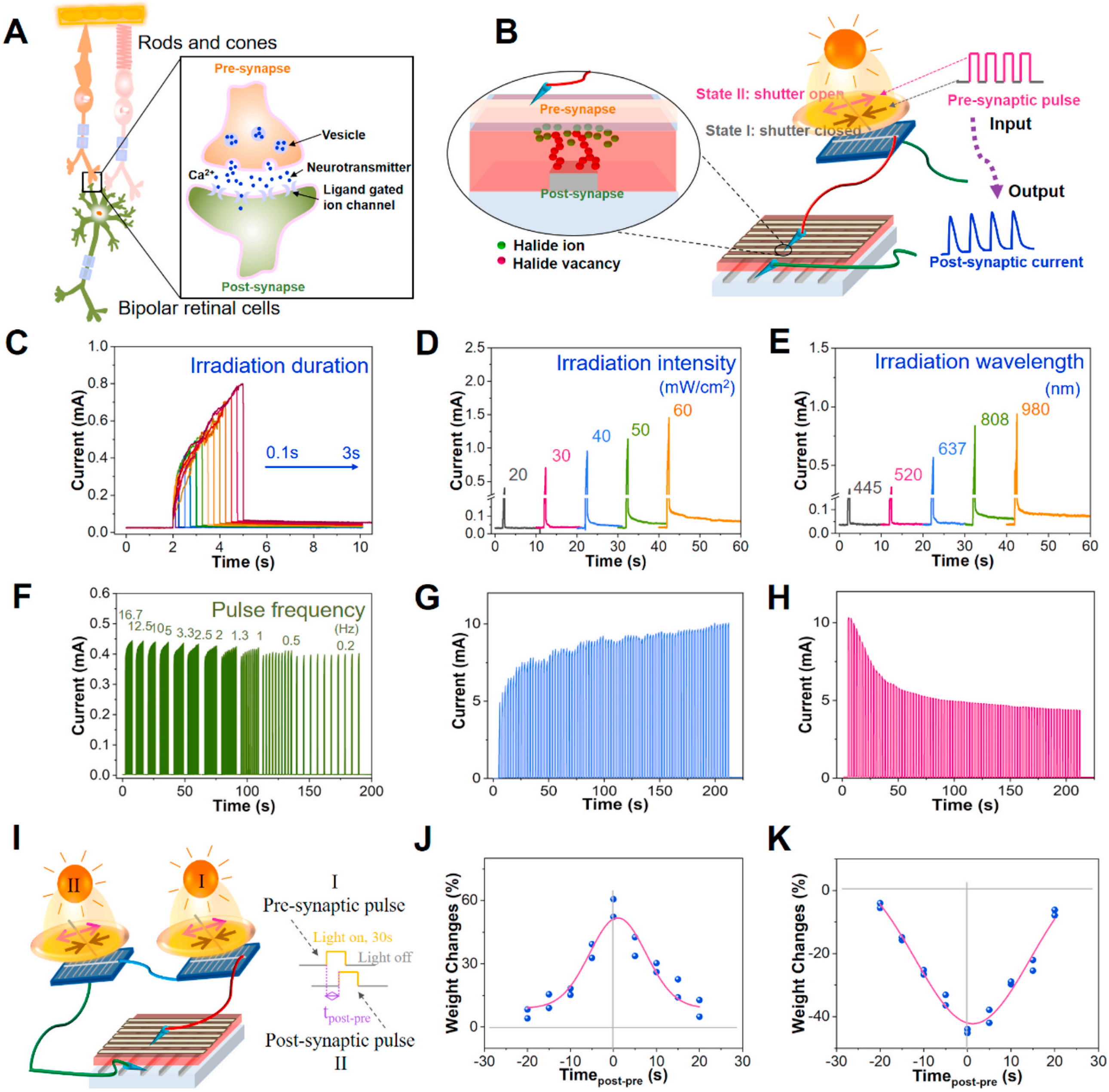

**Fig. 4.** Synaptic Plasticity of Artificial Synapses Powered by Solar Cells. (A) The schematic illustration of biological synapses between rods (or cones) and bipolar retinal cells. (B) The illustration of self-powered artificial synapses of the retina perception system based on halide perovskite memristors. (C) EPSC according to the irradiation duration from 0.1 to 3 s (irradiation intensity: 40 mW/cm$^2$). (D) EPSC according to the irradiation intensity (irradiation duration: 0.5 s). (E) EPSC according to the irradiation wavelength (irradiation intensity: 40 mW/cm$^2$; irradiation duration, 0.5 s). (F) EPSC according to the light irradiation frequency from 0.2 to 16.7 Hz (irradiation intensity, 40 mW/cm$^2$; irradiation duration, 0.5 s). (G) Emulated EPSC plasticity using the positive open-circuit voltage of photovoltaic cells (60 mW/cm$^2$, 0.1 s duration with 0.1 s interval). (H) Emulated EPSC plasticity using the negative open-circuit voltage (60 mW/cm$^2$, 0.1 s duration with 0.1 s interval). (I) The schematic diagram of our self-powered artificial retina perception system applied for STDP-like behaviors. Pre-synaptic and post-synaptic spikes are also given beside (irradiation intensity, 60 mW/cm$^2$). Implementation of STDP-like behaviors in our self-powered artificial retina perception system: (J) the symmetric Hebbian rule, and (K) the symmetric anti-Hebbian rule.

applied to self-driven artificial optic-neural synapses, and the expectant LTP was observed (Fig. S14). Next, the irradiation-intensity-dependent plasticity (IIDP) and irradiation-wavelength-dependent plasticity (IWDP) were also investigated for the self-driven artificial retina system. Fig. 4D and 4E shows the output current as the function of illumination intensity and wavelength, respectively. The EPSC increases as the increased irradiance from 20 to 60 mW/cm$^2$ and increased wavelength from 445 nm to 980 nm. By employing optical stimuli with relatively short wavelength and low intensity, the synaptic device is switched to a more conductive state, generates a current spike, and then decays to its initial state (STP). Conversely, the light illumination with high intensity and long wavelength gives rise to an enhanced synaptic strength with long relaxation time and a large spike current (LTP), since both $V_{oc}$ and short-circuit current density ($J_{sc}$) of silicon solar cell are improved (Fig. S12). According to the external quantum efficiency (EQE) of polycrystalline Si solar cells (Fig. S15), when irradiance is 40 mW/cm$^2$, numbers of photogenerated electrons in polycrystalline Si solar cells are calculated to be 7.6 × 10$^{16}$, 9.3 × 10$^{16}$, 1.14 × 10$^{17}$, 1.41 × 10$^{17}$, and 1.62 × 10$^{17}$ for input light of 445 (blue), 520 (green), 637 (red), 808 and 980 (NIR) nm, respectively (Table S2). This result indicates that stronger pre-synaptic spikes can be obtained under longer wavelength illumination, verifying the origin of IWDP as well as the redshift-enhanced-effect of synaptic strength for our self-driven artificial retina system. To preclude the memristive effect of photovoltaic cells for synaptic weight updating, the irradiation pulse was applied to a photovoltaic-cell-only circuit. The abrupt current drop without decay was observed in the photovoltaic-cell-only system (Fig. S16), so that the variation of synaptic weight is confirmed to be only originated from the conductance/resistance state change in perovskites memristor in our system. It should be noted that the changing trend of the photovoltage and the photocurrent are consistent for variable parameters of both irradiation intensities and irradiation wavelengths. Therefore, changes of both photovoltage and photocurrent of solar cells are beneficial to the resistance change of memristors and the achievement of synaptic plasticity of our artificial synapses.

We also examined the irradiation-frequency-dependent plasticity (0.2 to 16.7 Hz) for the self-driven artificial retina system (Fig. 4F and Fig. S17). The EPSC increases as the increased optical pulse frequency owing to the improved ion migration and the suppressed ion back-diffusion under the high-rate optical pulses. PPF index is calculated to be from 0.75% to 3.76%, as $\Delta t$ decreased from 5000 to 60 ms (Fig. S18). The time constants of the rapid and slow phases were fitted to be 0.207 and 3.228 s. Fig. 4G shows a continuous potentiation process of the EPSC with the accumulation of optical pulses, known as irradiation-number-dependent plasticity (INDP). When 100 light pulses (pulse magnitude, 60 mW/cm$^2$; pulse width, 1.0 s; pulse interval, 1.5 s) generate positive $V_{oc}$ (connected the back-aluminum/front-silver electrode of solar cells with the Ag/ITO electrode of memristors) was repeatedly applied, the EPSC exhibited strong enhancement from 4.9 to 10.1 mA. When the 100 optical pulses to generate negative $V_{oc}$ was applied (connected front-silver/back-aluminum electrode of the solar cell with Ag/ITO electrode of the memristor), the system presented continuous depression (Fig. 4H) with EPSC decreased from 10.3 to 4.4 mA.

Spike-time-dependent plasticity (STDP) rules were further emulated in the self-driven artificial retina system. The presynaptic spike applied to the Ag electrode and the postsynaptic spike applied to the ITO electrode were alternatively generated by two tandem silicon solar cells (Fig. 4I and Fig. S19). Two shutters are employed to control the time-sequence of presynaptic and postsynaptic spikes. When the shutter adjacent to Ag electrode is open and another shutter adjacent to ITO electrode is closed, the presynaptic spike will be generated by the solar cell under irradiation (spike magnitude, 50 mA/cm$^2$; spike width, 30 s), while another solar cell worked as a resistance (Fig. S20). After the setting time internal ($\Delta t > 0$), another shutter is opened to a produce postsynaptic spike applying to the ITO electrode. As a result, the symmetric Hebbian learning rule was realized, when the anode of the photovoltaic cell connected to the Ag electrode and the cathode connected to the ITO electrode (Fig. 4J). The symmetric anti-Hebbian learning rule was also verified, as the cathode of the photovoltaic cell connected to the Ag electrode and the anode connected to the ITO electrode (Fig. 4K). Weight changes in both symmetric Hebbian and anti-Hebbian learning cases were predominant, as intervals decreased. The largest weight change is also observed at the condition that two stimuli occurred simultaneously. The $\tau$ is calculated to be 6.5 and 13.1 s in the symmetric Hebbian and anti-Hebbian learning case, respectively.

### 3.5. *Self-powered artificial retina perception system and capabilities of image preprocessing*

In the process of artificial neural networks for pattern recognition, there are five different tasks for the image processing chain including image preprocessing, data reduction, segmentation, object recognition, and image understanding [8]. Among these tasks, the image preprocessing, one of the main characteristics of the biological retina, can realize perfect feature extraction and classification, and make a high image recognition rate with few epochs in the subsequent recognition process. CNNs are usually used to carry out image preprocessing, and attain pattern recognition with a postprocess of full connection [62,63]. Fig. 5A illuminates the recognition process of figure “4” by CNNs. Alternatively, our self-powered artificial retina perception system, consisting of solar cells and perovskite memristors, can realize the image preprocessing on the hardware level, and realize final pattern recognition with the assistance of ANNs (Fig. 5B). First, external optical signals are input into solar cell arrays (Fig. 5B: left hemisphere containing blue squares), converted into electrical signals (presynaptic spikes). Subsequently, perovskite memristor arrays receive presynaptic spikes (Fig. 5B: right hemisphere containing dark yellow squares), generate temporary memory information and proceed image preprocessing. Finally, the first-stage output image secondarily inputs ANNs and makes the final recognition via gradient descent iteration method.

The capacity of image preprocessing for our self-powered artificial retina perception system based on irradiation-intensity-dependent plasticity (IIDP) (Fig. 4D) was investigated. We employ 5 × 7 arrays (each cross point of the array is composed of one solar cell and one perovskite memristor, the equivalent circuit model is shown in Fig. S21) to receive external optical signals and carry out image memorizations. The photographic image of arrays is presented in Fig. S22. Input light intensities are set as 0 mW/cm$^2$ (marked I), 20 mW/cm$^2$ (marked II), 30 mW/cm$^2$ (marked III), 40 mW/cm$^2$ (marked IV) and 60 mW/cm$^2$ (marked V) on a solar simulator with an NREL-certified silicon reference cell. Thus, the input optical signals can be normalized to five pixels – 0, 0.3, 0.5, 0.7 and 1 which are demonstrated by devices I, devices II, devices III, devices IV, and devices V in the array, respectively (Fig. 6A: left). The heart-sharp pattern image was selected as optical signals to input to the array. After a training process (pulse width, 0.5 s; pulse interval, 0.5 s; pulse number, repeated 20 times; Fig. S23), EPSCs of the array can be obtained with a clear heart-sharp pattern as shown in Fig. 6A (middle), suggesting the capacity of image memorizations with enhanced contrast for our self-powered artificial retina perception system. However, there are still some noisy points in the image (eg. devices IV). After standing time lapses, EPSCs of devices stimulated by the weak intensity light decay faster compared with that of devices stimulated by the strong intensity light. After 50 s, the denoised effect of our self-powered artificial retina perception system is observed (Fig. 6A: right) in which the image contrast is further enhanced. After 2 min, almost all of noise points are removed and an expectant heart-sharp pattern becomes much clear (Fig. S24). These results imply that our self-powered artificial retina perception system has the capacity of image preprocessing containing both contrast enhancement and noise reduction, which is known as the feature extraction in CNNs.

Furthermore, 784 × 25 × 10 three-layered ANNs (software algorithm) was constructed and applied as the full connection for the image recognition without (Fig. S25a) and with (Fig. S25b) self-driven artificial optic-neural system. The relation between output currents and input light intensities was firstly established for our self-powered artificial retina perception system, according to the experimental results (Fig. S26). Then, an image of figures “1” - “9” was used for pattern recognition. The background noise signals of the image are composed of light signals with different intensities normalized in a range of 0–0.7 (Fig. 6B: left). After preprocessing via our self-driven artificial optic-neural system (hardware implementation), the result presents highlighted body features of figures and high-quality background noise reduction for the output image (Fig. 6B: right). Thus, recognition after preprocessing via our self-driven artificial optic-neural system can achieve a higher recognition rate of 86.55% within 180 training epochs, whereas directly recognizing in a three-layered full connection results recognition rate of 84.85% when training epochs run up to 480 (Fig. 6C). The image-recognition efficiency proves the quicker recognition speed and the higher recognition rate of ANNs with our self-powered artificial retina perception system. It should be noted that highlighted body-feature extraction also makes our system have the potential application as a smart detector for light [64].

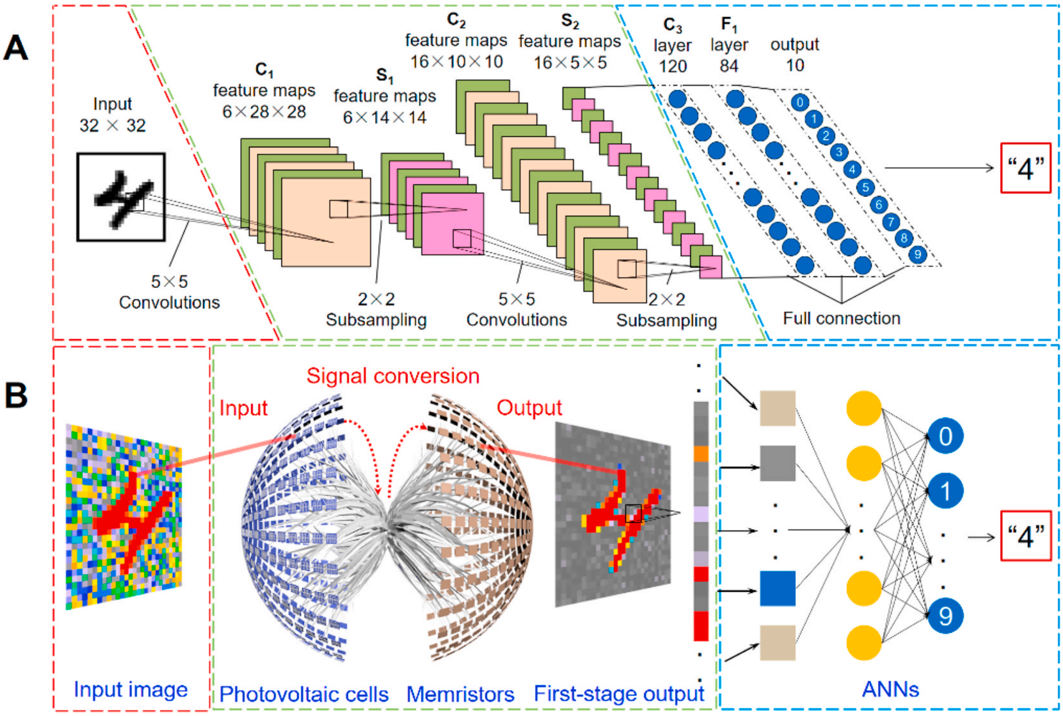

**Fig. 5.** Self-powered Artificial Retina Perception System. (A) The diagram of convolutional neural networks (CNNs). The input information was figure "4". (B) The illustration of the image preprocessing based on our self-powered artificial retina perception system and subsequent ANNs for image recognition.

Irradiation-wavelength-distinguishable image preprocessing is also realized by our self-powered artificial retina perception system. The training process was carried out under the 50 mW/cm$^2$ irradiation of 445 (blue), 520 (green), 637 (red) and 980 (NIR) nm (Fig. S27). The EPSC is highest under irradiation of 980 nm, suggesting that our system can highlight image body features via inputting NIR and reduce background noises of other wavelengths (Fig. S27). Then, the relation between EPSCs and input light wavelengths was established for our self-powered artificial retina perception system, according to the experimental results (Fig. S28). Then, an image of figures "1" - "9" was used for pattern recognition. The background noise signals of the image are composed of light signals with different wavelengths normalized in a range of 0–0.7 (Fig. S29: left). After preprocessing via our self-driven artificial optic-neural system, the output image presents highlighted body features of figures and good background noise reduction (Fig. S29: right). Thus, recognition after preprocessing via our self-driven artificial optic-neural system can achieve a higher recognition rate of 86.43% within 180 training epochs, whereas directly recognizing in a three-layered full connection results recognition rate of 82.07% when training epochs run up to 1260 (Fig. S30). Distinctly, our self-powered artificial retina perception system can improve both recognition speed and recognition rate for artificial neural networks, when the input image contains light signals of different wavelengths with the same intensity.

In real conditions, human retina can sense both light intensities and colors which is further emulated by our self-powered artificial retina system. Fig. 6D displays a 3D picture to present relations between postsynaptic currents and input light with various intensities and wavelengths. Then, an image of figures "1" - "9" was used for pattern recognition. The background noise signals of the image are composed of light signals with both different intensities and different wavelengths normalized in a range of 0–0.7 (Fig. 6E: left). After preprocessing via our self-driven artificial optic-neural system, the output image also presents highlighted body features of figures and good background noise reduction (Fig. 6E: right). Thus, recognition after preprocessing via our self-driven artificial optic-neural system can achieve a higher recognition rate of 85.63% within 180 training epochs, whereas directly recognizing in a three-layered full connection results recognition rate of 80.83% when training epochs run up to 1240 (Fig. S31). In addition, the recognition rate can be further improved in more complex fashion MNIST (Modified National Institute of Standards and Technology) image sets (Figs. S32 and S33) for our self-driven artificial optic-neural system. The final recognition rate can be improved from 77.31% (without our system) to 85.45% with our system (Fig. S33). These results indicate that our self-driven artificial optic-neural system can partly work as CNNs to attain feature extraction, and improve recognition rate, boost recognition speed, and reduce energy consumption.

## 4. Conclusions

In conclusion, we proposed a self-powered artificial retina system based on two-terminal silicon solar cells and halide perovskite memristors which is extendable to crossbar arrays for high-density integration. The P3HT-passivated perovskite memristor is advantageous over non-passivated memristor in its history-dependent resistance states and reliable state-maintenance capability, which allows reliable STP to LTP transition by controlling the duration/amplitude/frequency of input voltage. P3HT passivation not only influences the halogenic ion migration rate but also inhibits the reaction between the Ag electrode and the halogenic ion for the possible formation of silver halides. Utilizing this memristor as readout synapse, the self-powered artificial retina perception system was demonstrated converting the light wavelength and intensity information into analog, controllable EPSC signals. Moreover, our self-powered artificial retina system can realize contrast enhancement and noise reduction on the hardware level to partially implement the function of CNNs for feature extraction with improved recognition rate, boosted recognition speed, and reduced energy consumption. The proposed self-powered artificial retina system is expected to be introduced into the memory and computational center to detect and preprocess environmental condition for the next generation robotics and human-like sensory electronics for Internet of Things. Functions of self-powered and information-preprocessing will make this self-powered retina system have great potential for future artificial intelligence and

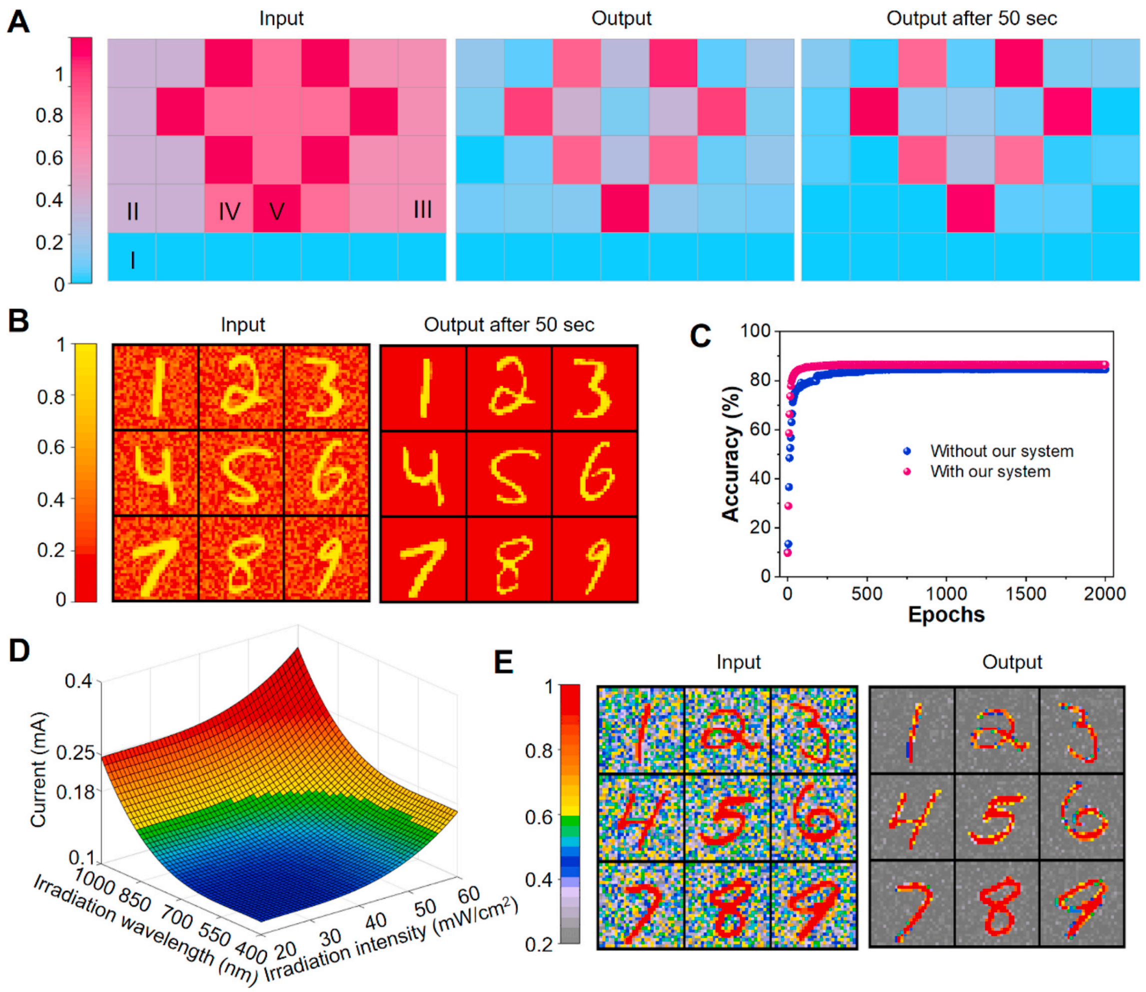

**Fig. 6.** Capabilities of Image Preprocessing. (A) The image contrast enhancement function of our self-powered artificial retina perception system when irradiation intensity was considered. Left: the input image with five pixels (I, 0 mW/cm$^2$; II, 20 mW/cm$^2$; III, 30 mW/cm$^2$; IV, 40 mW/cm$^2$; and V, 60 mW/cm$^2$). Middle: the output image of our self-driven artificial optic-neural system with a 5 × 7 array. Right: the output image after 50 s. Both input signals (light intensity) and output signals (current density) are normalized. (B) The contrast enhancement and the denoised effect of our self-powered artificial retina perception system when the irradiation intensity was considered. Left: the input image. Right: the output image after 50 s based on the fitting current-wavelength curve of our self-powered artificial retina perception system. (C) Comparisons of the image recognition rate with and without the image preprocessing based on our self-powered artificial retina perception system when the irradiation intensity was considered. (D) the 3D diagram of fitting current-wavelength-intensity curves of our self-powered artificial retina perception system. (E) The contrast enhancement and the denoised effect of our self-driven artificial optic-neural system when both irradiation wavelengths and intensities were considered. Left: the input image. Right: the output image based on the fitting current-wavelength-intensity curves of our self-powered artificial retina perception system.

robotics by reducing power consumption and improving integration density. Our self-powered artificial retina system also needs further improvement to work under weaker light via both the new design of device structure and the better choice of both low-operating-voltage memristors and high-open-circuit-voltage solar cells.

## CRediT authorship contribution statement

**Xiaoyang Yang:** Conceptualization, Validation, Investigation, Writing - original draft. **Ziyu Xiong:** Formal analysis, Methodology. **Yongji Chen:** Investigation. **Yi Ren:** Investigation. **Li Zhou:** Formal analysis, Investigation. **Huilin Li:** Investigation. **Ye Zhou:** Supervision, Project administration, Funding acquisition. **Feng Pan:** Investigation. **Su-Ting Han:** Supervision, Project administration, Funding acquisition, Writing - review & editing.

## Declaration of competing interest

The authors declare that they have no known competing financial interests or personal relationships that could have appeared to influence the work reported in this paper.

## Acknowledgements

X.Y. and Z.X. contributed equally to this work. X.Y. are grateful for the help from Dr. Jincheng Huang in Shenzhen University performing the EQE test of solar cells. The authors also acknowledge grants from the Natural Science Foundation of China (grant no. 61974093), Guangdong Province Special Support Plan for High-Level Talents (grant no. 2017TQ04X082), Guangdong Provincial Department of Science and Technology (grant no. 2018B030306028), and the Science and Technology Innovation Commission of Shenzhen (grant nos. JCYJ20180507182042530 and JCYJ20180507182000722).

## Appendix A. Supplementary data

Supplementary data to this article can be found online at https://doi.org/10.1016/j.nanoen.2020.105246.

## References

[1] Y. Lee, T.-W. Lee, Organic synapses for neuromorphic electronics: from brain-inspired computing to sensorimotor nervetronics, Acc. Chem. Res. 52 (2019) 964–974, https://doi.org/10.1021/acs.accounts.8b00553.

[2] C. Wan, P. Cai, M. Wang, Y. Qian, W. Huang, X. Chen, Artificial sensory memory, Adv. Mater. n/a (2019) 1902434, https://doi.org/10.1002/adma.201902434.

[3] R.K. Shepherd, M.N. Shivdasani, D.A.X. Nayagam, C.E. Williams, P.J. Blamey, Visual prostheses for the blind, Trends Biotechnol. 31 (2013) 562–571, https://doi.org/10.1016/j.tibtech.2013.07.001.

[4] F. Zhou, Z. Zhou, J. Chen, T.H. Choy, J. Wang, N. Zhang, Z. Lin, S. Yu, J. Kang, H.-S.P. Wong, Y. Chai, Optoelectronic resistive random access memory for neuromorphic vision sensors, Nat. Nanotechnol. 14 (2019) 776–782, https://doi.org/10.1038/s41565-019-0501-3.

[5] S.M. Kwon, S.W. Cho, M. Kim, J.S. Heo, Y.-H. Kim, S.K. Park, Environment-adaptable Artificial visual perception behaviors using a light-adjustable optoelectronic neuromorphic device array, Adv. Mater. 31 (2019) 1906433, https://doi.org/10.1002/adma.201906433.

[6] H. Wang, Q. Zhao, Z. Ni, Q. Li, H. Liu, Y. Yang, A ferroelectric/electrochemical modulated organic synapse for ultraflexible , artificial visual-perception system, Adv. Mater. 30 (2018) 1803961, https://doi.org/10.1002/adma.201803961.

[7] Y. Wang, M. Liu, J. Yang, G. Gui, Data-driven deep learning for automatic modulation recognition in cognitive radios, IEEE Trans. Veh. Technol. 68 (2019) 4074–4077, https://doi.org/10.1109/TVT.2019.2900460.

[8] M. Egmont-Petersen, D. de Ridder, H. Handels, Image processing with neural networks—a review, Pattern Recogn. 35 (2002) 2279–2301, https://doi.org/10.1016/S0031-3203(01)00178-9.

[9] Y. Ren, X. Yang, L. Zhou, J.-Y. Mao, S.-T. Han, Y. Zhou, Recent advances in ambipolar transistors for functional applications, Adv. Funct. Mater. 29 (2019) 1902105, https://doi.org/10.1002/adfm.201902105.

[10] S. Chen, Z. Lou, D. Chen, G. Shen, An artificial flexible visual memory system based on an UV-motivated memristor, Adv. Mater. 30 (2018) 1705400, https://doi.org/10.1002/adma.201705400.

[11] S.-F. Leung, K.-T. Ho, P.-K. Kung, V.K.S. Hsiao, H.N. Alshareef, Z.L. Wang, J.-H. He, A self-powered and flexible organometallic halide perovskite photodetector with very high detectivity, Adv. Mater. 30 (2018) 1704611, https://doi.org/10.1002/adma.201704611.

[12] T. Yang, Y. Zheng, Z. Du, W. Liu, Z. Yang, F. Gao, L. Wang, K.-C. Chou, X. Hou, W. Yang, Superior photodetectors based on all-inorganic perovskite CsPbI3 nanorods with ultrafast response and high stability, ACS Nano 12 (2018) 1611–1617, https://doi.org/10.1021/acsnano.7b08201.

[13] C. Choi, M.K. Choi, S. Liu, M.S. Kim, O.K. Park, C. Im, J. Kim, X. Qin, G.J. Lee, K.W. Cho, M. Kim, E. Joh, J. Lee, D. Son, S.-H. Kwon, N.L. Jeon, Y.M. Song, N. Lu, D.-H. Kim, Human eye-inspired soft optoelectronic device using high-density MoS2-graphene curved image sensor array, Nat. Commun. 8 (2017) 1664, https://doi.org/10.1038/s41467-017-01824-6.

[14] X. Wu, B. Zhou, J. Zhou, Y. Chen, Y. Chu, J. Huang, Distinguishable detection of ultraviolet, visible, and infrared spectrum with high-responsivity perovskite-based flexible photosensors, Small 14 (2018) 1800527, https://doi.org/10.1002/smll.201800527.

[15] Q. Li, J. van de Groep, Y. Wang, P.G. Kik, M.L. Brongersma, Transparent multispectral photodetectors mimicking the human visual system, Nat. Commun. 10 (2019) 4982, https://doi.org/10.1038/s41467-019-12899-8.

[16] F. Sun, Q. Lu, L. Liu, L. Li, Y. Wang, M. Hao, Z. Cao, Z. Wang, S. Wang, T. Li, T. Zhang, Bioinspired flexible, dual-modulation synaptic transistors toward artificial visual memory systems, Adv. Mater. Technol. 5 (2019) 1900888, https://doi.org/10.1002/admt.201900888.

[17] M. Kumar, T. Som, J. Kim, A transparent photonic artificial visual cortex, Adv. Mater. 31 (2019) 1903095, https://doi.org/10.1002/adma.201903095.

[18] Y. Lee, J.Y. Oh, W. Xu, O. Kim, T.R. Kim, J. Kang, Y. Kim, D. Son, J.B. Tok, M.J. Park, Stretchable organic optoelectronic sensorimotor synapse, Sci. Adv. 4 (2018), eaat7387.

[19] M. Patel, H.-S. Kim, J. Kim, Wafer-scale production of vertical SnS multilayers for high-performing photoelectric devices, Nanoscale 9 (2017) 15804–15812, https://doi.org/10.1039/C7NR03370B.

[20] C. Liu, X. Yan, X. Song, S. Ding, D.W. Zhang, P. Zhou, A semi-floating gate memory based on van der Waals heterostructures for quasi-non-volatile applications, Nat. Nanotechnol. 13 (2018) 404–410, https://doi.org/10.1038/s41565-018-0102-6.

[21] X. Pu, M. Liu, X. Chen, J. Sun, C. Du, Y. Zhang, J. Zhai, W. Hu, Z.L. Wang, Ultrastretchable, transparent triboelectric nanogenerator as electronic skin for biomechanical energy harvesting and tactile sensing, Sci. Adv. 3 (2017), e1700015, https://doi.org/10.1126/sciadv.1700015.

[22] K. Palczewski, Chemistry and biology of the initial steps in vision: the Friedenwald lecture, Invest. Ophthalmol. Vis. Sci. 55 (2014) 6651–6672, https://doi.org/10.1167/iovs.14-15502.

[23] H. Lorach, G. Goetz, R. Smith, X. Lei, Y. Mandel, T. Kamins, K. Mathieson, P. Huie, J. Harris, A. Sher, D. Palanker, Photovoltaic restoration of sight with high visual acuity, Nat. Med. 21 (2015) 476–482, https://doi.org/10.1038/nm.3851.

[24] L. Fang, S. Dai, Y. Zhao, D. Liu, J. Huang, Light-stimulated artificial synapses based on 2D organic field-effect transistors, Adv. Electron. Mater. (2019) 1901217, https://doi.org/10.1002/aelm.201901217.

[25] H. Li, X. Jiang, W. Ye, H. Zhang, L. Zhou, F. Zhang, D. She, Y. Zhou, S.-T. Han, Fully photon modulated heterostructure for neuromorphic computing, Nano Energy 65 (2019) 104000, https://doi.org/10.1016/j.nanoen.2019.104000.

[26] W. Xu, H. Cho, Y.-H. Kim, Y.-T. Kim, C. Wolf, C.-G. Park, T.-W. Lee, Organometal halide perovskite artificial synapses, Adv. Mater. 28 (2016) 5916–5922, https://doi.org/10.1002/adma.201506363.

[27] G.R. Neupane, A. Kaphle, P. Hari, Microwave-assisted Fe-doped ZnO nanoparticles for enhancement of silicon solar cell efficiency, Sol. Energy Mater. Sol. Cells 201 (2019) 110073, https://doi.org/10.1016/j.solmat.2019.110073.

[28] Z. Xiao, J. Huang, Energy-efficient hybrid perovskite memristors and synaptic devices, Adv. Electron. Mater. 2 (2016) 1600100, https://doi.org/10.1002/aelm.201600100.

[29] Y.-J. Chen, M.-J. Zhang, S. Yuan, Y. Qiu, X.-B. Wang, X. Jiang, Z. Gao, Y. Lin, F. Pan, Insight into interfaces and junction of polycrystalline silicon solar cells by kelvin probe force microscopy, Nano Energy 36 (2017) 303–312, https://doi.org/10.1016/j.nanoen.2017.04.045.

[30] W. Xiang, Z. Wang, D.J. Kubicki, W. Tress, J. Luo, D. Prochowicz, S. Akin, L. Emsley, J. Zhou, G. Dietler, M. Grätzel, A. Hagfeldt, Europium-Doped CsPbI$_2$Br for stable and highly efficient inorganic perovskite solar cells, Joule 3 (2019) 205–214, https://doi.org/10.1016/j.joule.2018.10.008.

[31] W. Chen, H. Chen, G. Xu, R. Xue, S. Wang, Y. Li, Y. Li, Precise control of crystal growth for highly efficient CsPbI$_2$Br perovskite solar cells, Joule 3 (2019) 191–204, https://doi.org/10.1016/j.joule.2018.10.011.

[32] Y. Park, J.-S. Lee, Artificial synapses with short- and long-term memory for spiking neural networks based on renewable materials, ACS Nano 11 (2017) 8962–8969, https://doi.org/10.1021/acsnano.7b03347.

[33] A. Swarnkar, A.R. Marshall, E.M. Sanehira, B.D. Chernomordik, D.T. Moore, J.A. Christians, T. Chakrabarti, J.M. Luther, Quantum dot–induced phase stabilization of α-CsPbI$_3$ perovskite for high-efficiency photovoltaics, Science 354 (80) (2016), https://doi.org/10.1126/science.aag2700, 92 LP – 95.

[34] Q. Lin, W. Hu, Z. Zang, M. Zhou, J. Du, M. Wang, S. Han, X. Tang, Transient resistive switching memory of CsPbBr3 thin films, Adv. Electron. Mater. 4 (2018) 1700596, https://doi.org/10.1002/aelm.201700596.

[35] M. Aamir, M. Sher, M.D. Khan, M.A. Malik, J. Akhtar, N. Revaprasadu, Controlled synthesis of all inorganic CsPbBr2I perovskite by non-template and aerosol assisted chemical vapour deposition, Mater. Lett. 190 (2017) 244–247, https://doi.org/10.1016/j.matlet.2017.01.013.

[36] L. Liu, P. Hu, Y. Li, W. An, J. Lu, W. Cui, P3HT-coated Ag3PO4 core-shell structure for enhanced photocatalysis under visible light irradiation, Appl. Surf. Sci. 466 (2019) 928–936, https://doi.org/10.1016/j.apsusc.2018.10.112.

[37] Y. Wang, Z. Lv, Q. Liao, H. Shan, J. Chen, Y. Zhou, L. Zhou, X. Chen, V.A.L. Roy, Z. Wang, Z. Xu, Y. Zeng, S. Han, Synergies of electrochemical metallization and valance change in all-inorganic perovskite quantum dots for resistive switching, Adv. Mater. 30 (2018) 1800327, https://doi.org/10.1002/adma.201800327.

[38] Y. Yuan, J. Huang, Ion migration in organometal trihalide perovskite and its impact on photovoltaic efficiency and stability, Acc. Chem. Res. 49 (2016) 286–293, https://doi.org/10.1021/acs.accounts.5b00420.

[39] C. Eames, J.M. Frost, P.R.F. Barnes, B.C. O'Regan, A. Walsh, M.S. Islam, Ionic transport in hybrid lead iodide perovskite solar cells, Nat. Commun. 6 (2015) 7497, https://doi.org/10.1038/ncomms8497.

[40] S.-I. Kim, Y. Lee, M.-H. Park, G.-T. Go, Y.-H. Kim, W. Xu, H.-D. Lee, H. Kim, D.-G. Seo, W. Lee, T.-W. Lee, Dimensionality dependent plasticity in halide perovskite artificial synapses for neuromorphic computing, Adv. Electron. Mater. 5 (2019) 1900008, https://doi.org/10.1002/aelm.201900008.

[41] J. Li, Q. Dong, N. Li, L. Wang, Direct evidence of ion diffusion for the silver-electrode-induced thermal degradation of inverted perovskite solar cells, Adv. Energy Mater. 7 (2017) 1602922, https://doi.org/10.1002/aenm.201602922.

[42] B. Li, Y. Zhang, L. Fu, T. Yu, S. Zhou, L. Zhang, L. Yin, Surface passivation engineering strategy to fully-inorganic cubic CsPbI3 perovskites for high-performance solar cells, Nat. Commun. 9 (2018) 1076, https://doi.org/10.1038/s41467-018-03169-0.

[43] P.A. Merolla, J.V. Arthur, R. Alvarez-Icaza, A.S. Cassidy, J. Sawada, F. Akopyan, B.L. Jackson, N. Imam, C. Guo, Y. Nakamura, B. Brezzo, I. Vo, S.K. Esser, R. Appuswamy, B. Taba, A. Amir, M.D. Flickner, W.P. Risk, R. Manohar, D.S. Modha, A million spiking-neuron integrated circuit with a scalable communication network and interface, Science 345 (2014) 668–673, https://doi.org/10.1126/science.1254642.

[44] S. Song, K.D. Miller, L.F. Abbott, Competitive Hebbian learning through spike-timing-dependent synaptic plasticity, Nat. Neurosci. 3 (2000) 919–926, https://doi.org/10.1038/78829.

[45] C. Zhang, W. Bin Ye, K. Zhou, H.-Y. Chen, J.-Q. Yang, G. Ding, X. Chen, Y. Zhou, L. Zhou, F. Li, S.-T. Han, Bioinspired artificial sensory nerve based on nafion memristor, Adv. Funct. Mater. 29 (2019) 1808783, https://doi.org/10.1002/adfm.201808783.

[46] J.T. Yang, C. Ge, J.Y. Du, H.Y. Huang, M. He, C. Wang, H. Bin Lu, G.Z. Yang, K.J. Jin, Artificial synapses emulated by an electrolyte-gated tungsten-oxide transistor, Adv. Mater. 30 (2018) 1801548, https://doi.org/10.1002/adma.201801548.

[47] F. Yu, L.Q. Zhu, H. Xiao, W.T. Gao, Y.B. Guo, Restickable oxide neuromorphic transistors with spike-timing-dependent plasticity and Pavlovian associative learning activities, Adv. Funct. Mater. 28 (2018) 1804025, https://doi.org/10.1002/adfm.201804025.

[48] L.F. Abbott, S.B. Nelson, Synaptic plasticity: taming the beast, Nat. Neurosci. 3 (2000) 1178–1183, https://doi.org/10.1038/81453.

[49] R.A. John, N. Yantara, Y.F. Ng, G. Narasimman, E. Mosconi, D. Meggiolaro, M.R. Kulkarni, P.K. Gopalakrishnan, C.A. Nguyen, F. De Angelis, S.G. Mhaisalkar, A. Basu, N. Mathews, Ionotronic halide perovskite drift-diffusive synapses for low-power neuromorphic computation, Adv. Mater. 30 (2018) 1805454, https://doi.org/10.1002/adma.201805454.

[50] Y. Li, Y. Zhong, L. Xu, J. Zhang, X. Xu, H. Sun, X. Miao, Ultrafast synaptic events in a chalcogenide memristor, Sci. Rep. 3 (2013) 1619, https://doi.org/10.1038/srep01619.

[51] L. Zhou, S. Yang, G. Ding, J.-Q. Yang, Y. Ren, S.-R. Zhang, J.-Y. Mao, Y. Yang, Y. Zhou, S.-T. Han, Tunable synaptic behavior realized in C3N composite based memristor, Nano Energy 58 (2019) 293–303, https://doi.org/10.1016/j.nanoen.2019.01.045.

[52] Q. Zheng, B. Shi, Z. Li, Z.L. Wang, Recent progress on piezoelectric and triboelectric energy harvesters in biomedical systems, Adv. Sci. 4 (2017) 1700029, https://doi.org/10.1002/advs.201700029.

[53] L. Li, Z. Chen, M. Hao, S. Wang, F. Sun, Z. Zhao, T. Zhang, Moisture-driven power generation for multifunctional flexible sensing systems, Nano Lett. 19 (2019) 5544–5552, https://doi.org/10.1021/acs.nanolett.9b02081.

[54] A.J. Bandodkar, J. Wang, Wearable biofuel cells: a review, Electroanalysis 28 (2016) 1188–1200, https://doi.org/10.1002/elan.201600019.

[55] C. Wan, R. Tian, A.B. Azizi, Y. Huang, Q. Wei, R. Sasai, S. Wasusate, T. Ishida, K. Koumoto, Flexible thermoelectric foil for wearable energy harvesting, Nano Energy 30 (2016) 840–845, https://doi.org/10.1016/j.nanoen.2016.09.011.

[56] R. Liu, J. Wang, T. Sun, M. Wang, C. Wu, H. Zou, T. Song, X. Zhang, S.-T. Lee, Z. L. Wang, B. Sun, Silicon nanowire/polymer hybrid solar cell-supercapacitor: a self-charging power unit with a total efficiency of 10.5%, Nano Lett. 17 (2017) 4240–4247, https://doi.org/10.1021/acs.nanolett.7b01154.

[57] P. Du, X. Hu, C. Yi, H.C. Liu, P. Liu, H.-L. Zhang, X. Gong, Self-powered electronics by integration of flexible solid-state graphene-based supercapacitors with high performance perovskite hybrid solar cells, Adv. Funct. Mater. 25 (2015) 2420–2427, https://doi.org/10.1002/adfm.201500335.

[58] X. Chen, H. Sun, Z. Yang, G. Guan, Z. Zhang, L. Qiu, H. Peng, A novel "energy fiber" by coaxially integrating dye-sensitized solar cell and electrochemical capacitor, J. Mater. Chem. A. 2 (2014) 1897–1902, https://doi.org/10.1039/C3TA13712K.

[59] S. Park, S.W. Heo, W. Lee, D. Inoue, Z. Jiang, K. Yu, H. Jinno, D. Hashizume, M. Sekino, T. Yokota, K. Fukuda, K. Tajima, T. Someya, Self-powered ultra-flexible electronics via nano-grating-patterned organic photovoltaics, Nature 561 (2018) 516–521, https://doi.org/10.1038/s41586-018-0536-x.

[60] K. Kang, H. Ahn, Y. Song, W. Lee, J. Kim, Y. Kim, D. Yoo, T. Lee, High-performance solution-processed organo-metal halide perovskite unipolar resistive memory devices in a cross-bar array structure, Adv. Mater. 31 (2019) 1804841, https://doi.org/10.1002/adma.201804841.

[61] M.J. Kerr, A. Cuevas, Generalized analysis of the illumination intensity vs. open-circuit voltage of solar cells, Sol. Energy 76 (2004) 263–267, https://doi.org/10.1016/j.solener.2003.07.027.

[62] Y.-D. Zhang, Z. Dong, X. Chen, W. Jia, S. Du, K. Muhammad, S.-H. Wang, Image based fruit category classification by 13-layer deep convolutional neural network and data augmentation, Multimed. Tool. Appl. 78 (2019) 3613–3632, https://doi.org/10.1007/s11042-017-5243-3.

[63] N. Takemura, Y. Makihara, D. Muramatsu, T. Echigo, Y. Yagi, On input/output architectures for convolutional neural network-based cross-view gait recognition, IEEE Trans. Circ. Syst. Video Technol. 29 (2019) 2708–2719, https://doi.org/10.1109/TCSVT.2017.2760835.

[64] H.-L. Park, H. Kim, D. Lim, H. Zhou, Y.-H. Kim, Y. Lee, S. Park, T.-W. Lee, Retina-inspired carbon nitride-based photonic synapses for selective detection of UV light, Adv. Mater. 32 (2020) 1906899, https://doi.org/10.1002/adma.201906899.

**Dr. Xiaoyang Yang** is currently a postdoctoral researcher at Shenzhen University. He received his PhD degree in Mechanics (Advanced Materials and Mechanics) in 2018 from Peking University, China. His research interests located in storage mechanism and novel materials (e.g. organic, inorganic and hybrid semiconductors and nanomaterials) for memory devices, such as data storage, artificial synapse devices and sensors.

**Ziyu Xiong** received the B.S. degree in college of Science, University of Science and Technology Liaoning, Liaoning, China. He currently is working toward the M.S. degree at College of Physics and Optoelectronic Engineering, Shenzhen University, Shenzhen, China. His research interests include data storage, artificial synapse devices, and machine learning.

**Yong-Ji Chen** received his Bachelor's degree (BE) from ShiHeZi University, China, in 2014. He is currently a PHD student in the School of Advanced Materials, Peking University, China. His main research interests include polycrystalline silicon solar cells.

**Yi Ren** received his physics bachelor's degree from Institute for Advanced Study at Shenzhen University, Guangdong, China, in 2018. He is now a postgraduate student of Institute for Advanced Study in Shenzhen University. His research interests include organic/inorganic materials for nanoscale devices, such as data storage and artificial synapse devices.

**Dr. Li Zhou** is currently an associate research fellow at Shenzhen University. She received her PhD degree in Materials Science and Engineering from City University of Hong Kong (2016). Her research interests include organic/inorganic semiconductors and nanostructured materials for nano-scale devices, such as data storage and artificial synapse devices.

**Dr. Huilin Li** is currently an associate research fellow at Shenzhen University. He received his PhD degree from University of Science and Technology of China in 2017. His research interests located in nanomaterials (e.g. quantum dots, semiconductor and mental nanomaterials) for memory devices, such as data storage and artificial synapse devices.

**Prof. Ye Zhou** is an IAS Fellow at the Institute for Advanced Study, Shenzhen University. His research interests include flexible and printed electronics, organic/inorganic semiconductors, surface and interface physics, nanostructured materials, and nano-scale devices for technological applications, such as logic circuits, data storage, photonics and sensors.

**Prof. Feng Pan** National 1000-plan Professor, Founding Dean of School of Advanced Materials, Peking University Shenzhen Graduate School, Director of National Center of Electric Vehicle Power Battery and Materials for International Research, got B.S. from Dept. Chemistry, Peking University in1985 and PhD from Dept. of P&A Chemistry, University of Strathclyde, Glasgow, UK, with "Patrick D. Ritchie Prize" for the best Ph.D. in 1994. With more than a decade experience in large international incorporations, Prof. Pan has been engaged in fundamental research and product development of novel optoelectronic and energy storage materials and devices.

**Prof. Su-Ting Han** is an associate professor at Shenzhen University. She received her MSc degree in Analytical Chemistry from Hong Kong Baptist University and her PhD degree in Physics and Materials Science from City University of Hong Kong. After graduation, she worked at the City University of Hong Kong as a postdoctoral fellow. Her research interests include functional electronic devices and flexible, stretchable, and wearable electronics.